Two-step quantum cutting efficiency in Pr^{3+}-Yb^{3+} codoped KY_3F_{10}

D. Serrano, A. Braud,* J. L. Doualan, W. Bolaños, R. Moncorgé, and P. Camy
Centre de Recherche sur les Ions, les Matériaux et la Photonique (CIMAP) UMR 6252CEA-CNRS-ENSICAEN-Université de Caen, 6 Bvd du Maréchal Juin 14050 Caen, France

(Received 26 August 2013; revised manuscript received 23 October 2013; published 27 November 2013)

The efficiency of a two-step quantum cutting (QC) mechanism for solar downconversion via two consecutive energy transfers from Pr^{3+} to Yb^{3+} is investigated in Pr^{3+}-Yb^{3+} codoped KY_3F_{10} crystals. The efficiency of the QC second energy transfer involving the Pr^{3+} ($^1G_4$) and Yb^{3+} ($^2F_{5/2}$) levels is particularly difficult to determine in a precise manner since these two levels are coupled by reciprocal energy transfer. We present a specific rate equation modeling that accurately describes Pr^{3+} and Yb^{3+} dynamics and intensity ratios measured as a function of the Yb^{3+} concentration. The modeling enables to calculate energy transfer rates for all the processes and shows the competition between the two-step QC mechanism and parasitic processes. The first-step of the QC mechanism is, as expected, particularly efficient reaching 96.9% and is not challenged by competing processes. The second step of the QC, while reaching an intrinsic efficiency of 75.9%, is plagued by backtransfers from Yb^{3+} ($^2F_{5/2}$) to Pr^{3+} ($^1G_4$) along with efficient concentration quenching mechanisms draining the Yb^{3+} excited-state. In addition, the investigation of intensity ratios with the Yb^{3+} concentration shows the importance of energy migration among Yb^{3+} ions that further enhances the detrimental effect of the Yb^{3+} quenching processes. As a result, the intrinsic QC efficiency (QCE) of the QC first and second energy transfers increases with the Yb^{3+} doping level up to 173% in KY_3F_{10}: 0.5%Pr^{3+}-20%Yb^{3+}, while the real QCE reduced by migration-assisted quenching processes is only 6.2% in this sample. These results clarify apparently conflicting reports found in the literature showing, on one hand, very high QCEs derived from spectroscopic experiments and, on the other hand, very low efficiency values obtained from integrating sphere measurements.

DOI: 10.1103/PhysRevB.88.205144 PACS number(s): 78.20.−e, 78.55.−m

I. INTRODUCTION

The conversion efficiency of photovoltaic devices, such as Si solar cells, is limited by several factors, such as reflection losses, charge carrier separation efficiency, and conduction efficiency. While these factors are important, the issue of spectral losses at a more fundamental level is crucial and must be addressed in detail. These spectral losses are characterized by the inadequate exploitation of the solar spectrum that prevents Si cells overcoming the theoretical upper efficiency limit set around 30% for a single junction.[1] Two types of spectral losses exist, depending on the incoming solar photon wavelength. First, the semiconductor transparency to below-band-gap photons makes these low-energy photons useless for energy conversion. Second, the thermalization of excited carriers within the conduction band following above-band-gap photons absorption represents a loss of energy and furthermore a source of heat that deteriorates the solar cell performance. These thermalization losses can be advantageously reduced by implementing quantum cutting (QC) layers into existing photovoltaic (PV) modules. The purpose of these QC materials is to absorb uv and/or visible photons, splitting them into two or more near-infrared (NIR) photons, which can be then absorbed by the semiconducting active layer in order to generate several electron-hole pairs per incident photon.[2] Most systems exhibiting the conversion of a single incoming photon into the emission of multiple photons consist of materials doped with one or several types of impurity ions. Early examples of quantum cutters resulted from research on new phosphors for mercury-free fluorescent tubes and plasma display panels. Efficient QC was thus demonstrated to convert vacuum ultraviolet (VUV) radiation into visible light with rare-earth-doped materials, such as Eu^{3+}: $LiGdF_4$ (Ref. 3, 4) and Gd^{3+}-Eu^{3+}: BaF_2 (Ref. 5).

Among rare-earth ions, trivalent ytterbium is an optimal candidate as a QC emitter for Si-based PV technologies since it has a single excited state around 10 000 cm^{-1} (1.24 eV), matching the silicon band-gap energy (1.12 eV), which means that the infrared Yb^{3+} emission can be efficiently absorbed by silicon solar cells without significant thermalization losses. The choice of a suitable donor ion able to absorb high-energy photons and to transfer its energy to at least two Yb^{3+} ions appears, nevertheless, complicated. Ions such as Nd^{3+} (Ref. 6), Er^{3+} (Ref. 7), Pr^{3+} (Ref. 8), Tm^{3+} (Refs. 9, 10), and Tb^{3+} (Ref. 11) have been considered for visible to NIR QC with Yb^{3+} ions. Two consecutive energy transfers can take place from one donor to two Yb^{3+} ions when using as donor Nd^{3+}, Er^{3+}, or Pr^{3+}. The QC mechanism is then a true two-step process, while the simultaneous excitation of two Yb^{3+} ions occurs by a single cooperative energy transfer when using Tb^{3+} ions as donors. Two-step processes are intrinsically more efficient since they are based on direct donor-acceptor energy transfers, which are 4 or 5 orders of magnitude more effective than second-order cooperative mechanisms.[12] Among previously mentioned codopings, the Pr^{3+}-Yb^{3+} couple is often considered as particularly promising. Praseodymium is an interesting candidate to transfer its energy to neighboring Yb^{3+} ions since, as displayed in Fig. 1. The $^3P_0$ metastable energy level is located at 20 000 cm^{-1} approximately and $^1G_4$ around 10 000 cm^{-1}, which makes possible a QC mechanism based on two resonant energy transfers: Pr^{3+}($^3P_0 \rightarrow {}^1G_4$) to Yb^{3+}($^2F_{7/2} \rightarrow {}^2F_{5/2}$) and Pr^{3+}($^1G_4 \rightarrow {}^3H_4$) to Yb^{3+}($^2F_{7/2} \rightarrow {}^2F_{5/2}$). In addition, in contrast to other codopings, such as Er^{3+}-Yb^{3+} or Nd^{3+}-Yb^{3+}, the energy gap between the $^3P_0$ and $^1G_4$ levels and their immediate lower energy levels ($^1D_2$ and $^3F_4$, respectively) is large enough (Fig. 1) to reduce the negative impact of multiphonon relaxation. Multiphonon transitions can

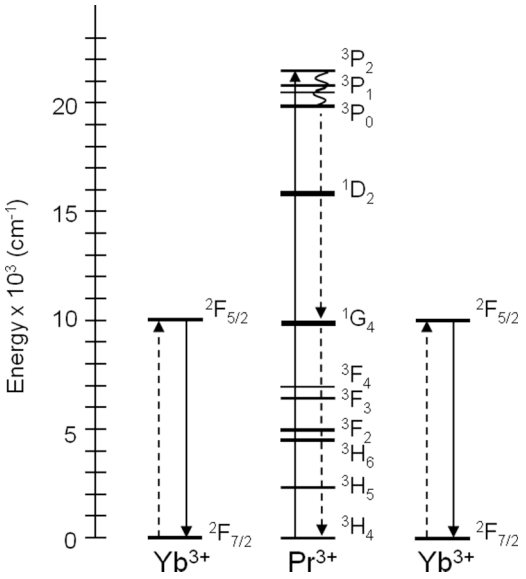

FIG. 1. Schematic representation of the quantum cutting mechanism with Pr^{3+} and Yb^{3+} ions.

be even neglected in the Pr^{3+}-Yb^{3+} system when using low phonon energy host materials, such as fluorides.

When evaluating a system based on energy transfers for potential applications, as is the case with the solar quantum cutter, an accurate determination of the efficiency of the different energy transfers involved in the mechanism becomes essential. The efficiency of the first step of the QC process or Pr^{3+} ($^3P_0 \rightarrow {}^1G_4$) to Yb^{3+} ($^2F_{7/2} \rightarrow {}^2F_{5/2}$) can be derived from the evolution of the $^3P_0$ fluorescence decay with the Yb^{3+} content.[13] High energy transfer efficiencies (ETEs) have been reported for this first energy transfer in various Pr^{3+}-Yb^{3+} doped materials, such as SrF_2,[8] CaF_2,[14] LaF_3,[15] $LiYF_4$,[16] $GdAl_3(BO_3)_4$,[17] La_2BaZnO_5[18], and glasses.[19] In contrast, the efficiency of the QC second step, $Pr^{3+}(^1G_4 \rightarrow {}^3H_4)$ to $Yb^{3+}(^2F_{7/2} \rightarrow {}^2F_{5/2})$, has been far less investigated. Moreover, the few experimental studies performed so far seem to lead to apparently contradictory conclusions with results based on excitation spectroscopy, suggesting an efficient second step,[8,20] while integrating sphere measurements indicate that the real quantum cutting efficiency (QCE) is as low as 12%.[21] It is clear that the efficiency of the QC second energy transfer is rather complicated to determine since the $^1G_4$ emission depends at the same time on both the $Pr^{3+}(^1G_4 \rightarrow {}^3H_4)$ to $Yb^{3+}(^2F_{7/2} \rightarrow {}^2F_{5/2})$ energy transfer and the reciprocal $Yb^{3+}(^2F_{5/2} \rightarrow {}^2F_{7/2})$ to $Pr^{3+}(^3H_4 \rightarrow {}^1G_4)$ backtransfer.[22] Interestingly, this situation is rather similar to the case of the Tm^{3+}-Ho^{3+}codoping in which $Tm^{3+}(^3F_4)$ and $Ho^{3+}(^5I_7)$ are coupled through back and forth energy transfers creating an equilibrium between the two levels.[23]

In this paper, we present a comprehensive analysis of the two-step QC process in Pr^{3+}-Yb^{3+}codoped KY_3F_{10}, and for the first time, to the best of our knowledge, a detailed investigation of the QC second ETE. The doping of KY_3F_{10} with rare-earth ions has been reported in several publications.[24–27] KY_3F_{10} crystallizes in a cubic system with a lattice parameter of 11.536 Å and $Fm3m$ as spatial group. In this structure, each rare-earth ion is surrounded by eight fluorines, forming a square-based antiprism of C_{4v} symmetry. As a fluoride material, its relatively low phonon energy (420 cm^{-1}) makes it particularly suitable for applications involving energy transfers. In order to have a detailed understanding of the downconversion QC mechanism in KY_3F_{10}: Pr^{3+}-Yb^{3+}, two sets of experiments were carried out. On the one hand, the evolution of the praseodymium emission intensities from $^3P_0$ and $^1G_4$, as well as the downconverted ytterbium emission intensity were investigated as a function of the Yb^{3+} concentration upon $Pr^{3+}(^3P_2)$ excitation at 442 nm and by pumping Yb^{3+} ions at 940 nm. This series of experiments provides extra information about the QC second step, $Pr^{3+}(^1G_4 \rightarrow {}^3H_4)$ to $Yb^{3+}(^2F_{7/2} \rightarrow {}^2F_{5/2})$, as well as the reciprocal $Yb^{3+}(^2F_{5/2} \rightarrow {}^2F_{7/2})$ to $Pr^{3+}(^3H_4 \rightarrow {}^1G_4)$ energy transfer. A second set of experiments was performed under pulsed excitation both at 442 and 940 nm in order to retrieve the $^3P_0$, $^1G_4$, and Yb^{3+} decay curves. A single set of energy transfer parameters was used within a rate equation model to describe the experimental results both in pulsed and continuous wave (CW) regimes. This comprehensive modeling of the Pr^{3+}-Yb^{3+} two-step QC system shows, in particular, the rather high efficiency of the QC second step but also the tremendous impact of parasitic migration-assisted quenching processes on the overall QC efficiency.

II. METHODS

A series of KY_3F_{10} single crystals codoped with Pr^{3+} (0.5%at.) and Yb^{3+} (0, 5, 10, and 20%at.) were grown in our laboratory by using the Bridgman-Stockbarger technique. Pure KF, YF_3, PrF_3, and YbF_3 powders were used as raw materials. The details of the growth procedure can be found in Ref. 28. The final dopant concentrations in the crystals were measured by the inductively coupled plasma technique and confirmed by absorption measurements using calibrated reference samples. Both methods demonstrated real concentrations very close to the nominal concentrations in the melt. Afterwards, the crystals were prepared as powder samples for spectroscopic experiments. Pr^{3+} ions were excited into the $^3P_2$ level with a blue GaN diode laser emitting at 442 nm, while Yb^{3+} ions were pumped at 940 nm ($^2F_{5/2}$) using a Ti:Sapphire laser. The sample fluorescence was dispersed by a 0.5 m monochromator and detected by using a standard lock-in amplifier technique associated with a photomultiplier tube or InGaAs photodiode for signal detection. Emission decays and time-resolved spectra were carried out by using an optical parametric oscillator pumped by the third harmonic (355 nm) of a Q-switched Nd:YAG laser. After dispersion by a 0.25 m monochromator, the luminescent transient signals obtained after pulsed excitation, were fed into a digital oscilloscope and averaged out to improve the signal-to-noise ratio. All the experimental recordings were corrected afterwards from the setup spectral response.

III. EXPERIMENTAL RESULTS

Once excited at 442 nm, Pr^{3+} ions in the $^3P_2$ level undergo fast multiphonon relaxation down to $^3P_0$. Typical Pr^{3+}-Yb^{3+} codoped KY_3F_{10} fluorescence spectra displayed in Fig. 2 show the main transitions from the $^3P_0$ level. The large band around

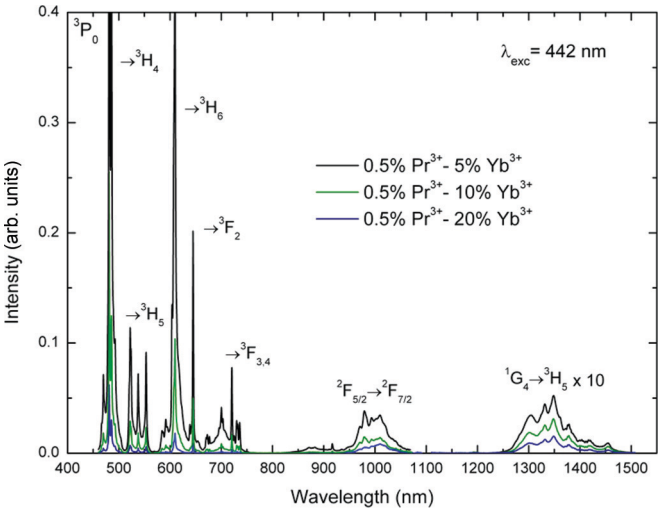

FIG. 2. (Color online) Room-temperature emission spectra under laser diode excitation at 442 nm in KY_3F_{10} codoped with 0.5%Pr^{3+}-5%Yb^{3+} (black); 0.5%Pr^{3+}-10%Yb^{3+} (green), and 0.5%Pr^{3+}-20%Yb^{3+} (blue).

1 μm is assigned to the $^2F_{5/2} \rightarrow {}^2F_{7/2}$ Yb^{3+} emission and the weak band around 1.3 μm is identified as the $^1G_4 \rightarrow {}^3H_5$ Pr^{3+} transition. The NIR emission from Yb^{3+} under blue excitation at 442 nm already constitutes first evidence of Pr^{3+} to Yb^{3+} energy transfer.

A direct comparison of the evolution of the emission spectra with the Yb^{3+} content could be performed since the excitation and detection geometry were kept identical for all samples, and all these samples were prepared as powders, having the same geometry. As expected for a single-site structure, the shape of the Pr^{3+} spectra ($^3P_0$ and $^1G_4$) remains the same even for a high Yb^{3+} concentration (20%), indicating that the Yb^{3+} doping does not distort the Pr^{3+} incorporation site.[13] An important quenching of the luminescence intensity is globally observed in Fig. 2 when the Yb^{3+} content increases. While the quenching of $^3P_0$ can be directly related to the depopulation of this energy level by the first energy transfer, the Yb^{3+} quenching is usually associated with concentration-related processes resulting in the draining of the Yb^{3+} excited state. At high Yb^{3+} contents, concentration quenching due to energy migration among the Yb^{3+} ions followed by energy transfer to defects or other impurities (quenching centers) is a well-known mechanism already reported in Yb^{3+} singly doped KY_3F_{10}.[27] Considering, finally, the $^1G_4$ emission spectra at 1.3 μm (Fig. 2), the emission intensity is also observed to decrease with the Yb^{3+} concentration. The quenching of the $^1G_4$ emission can be related, in principle, to the QC second step Pr^{3+} ($^1G_4 \rightarrow {}^3H_4$) to Yb^{3+} ($^2F_{7/2} \rightarrow {}^2F_{5/2}$), leading to the excitation of a second Yb^{3+} ion. This result is a first indication that the QC second step energy transfer does take place despite that the backtransfer from Yb^{3+} to Pr^{3+} is more probable because of simple thermodynamic considerations. Indeed, the $^1G_4$ level is at lower energy than the $^2F_{5/2}$ level. Therefore, the backtransfer is more likely to occur than the QC second-step energy transfer. However, this thermodynamic point of view does not encompass the acceptor concentrations, which are very different for both energy transfers. In a 0.5%Pr^{3+}-20%Yb^{3+}: KY_3F_{10} sample, the acceptor concentration (Yb^{3+}) for the Pr^{3+} to Yb^{3+} QC second-step energy transfer is 40 times larger than for the reverse mechanism. A larger acceptor concentration increases the corresponding energy transfer rate and can therefore compensate for the smaller spectral overlap, which characterizes the QC second-step energy transfer. As a consequence, the back and forth energy transfer between $^1G_4$ and $^2F_{5/2}$ contributes to the $^1G_4$ emission, which makes the analysis more complex.

For further insight into the effects of the first energy transfer, second energy transfer and back-transfer, the evolutions of the Pr^{3+} and Yb^{3+} emissions with the Yb^{3+} concentration are compared by normalizing either the $^3P_0$ or $^1G_4$ emissions (Fig. 3). As shown in Fig. 3(a), under excitation at 442 nm, the Yb^{3+} emission increases in comparison with the $^3P_0$ emission when increasing the Yb^{3+} concentration. This can be explained by the increasing efficiency of the first energy transfer. On the opposite, the Yb^{3+} emission decreases in comparison with the $^1G_4$ emission [Fig. 3(b)] whether the excitation occurs at 940 nm (Yb^{3+}) or at 442 nm (Pr^{3+}). This would indicate that not only the backtransfer depletes the Yb^{3+}($^2F_{5/2}$) level but also other possible quenching mechanisms.

The $^3P_0$, $^1G_4$, and Yb^{3+} fluorescence decays are presented in Fig. 4, and the corresponding fluorescence lifetimes are summarized in Table I. Due to the slight nonexponential character of the decay curves, average $^3P_0$ lifetimes were determined by integrating the entire decay curves according to the expression:

$$\tau = \frac{1}{I_0} \int_0^\infty I(t)dt, \tag{1}$$

where I_0 is the fluorescence intensity at $t = 0$.

The study of the dynamics shows a decrease of all lifetimes with the Yb^{3+} content for the $^3P_0$, $^1G_4$, and $^2F_{5/2}$ energy levels, upon both 442- and 940-nm excitations. This result is consistent with the emission intensity decrease previously observed in Fig. 2. Special care was taken in the case of the Yb^{3+} excitation at 940 nm to keep the excitation density at a low level in order to avoid possible upconversion phenomena between Pr^{3+} and Yb^{3+} ions in their $^1G_4$ and $^2F_{5/2}$ levels, which would affect their fluorescence dynamics. As mentioned earlier, the $^3P_0$ lifetime decrease is due to the first energy transfer, while backtransfer processes participate in the quenching of the Yb^{3+} emission intensity and lifetime. The decrease of the $^1G_4$ lifetime (Fig. 4) is another indication that the QC second step from the Pr^{3+} ($^1G_4$) towards Yb^{3+} ions takes place, despite previously discussed thermodynamic considerations. If this Pr^{3+} ($^1G_4$) towards Yb^{3+} energy transfer did not take place, one should see in the simple case of Yb^{3+} excitation at 940 nm a rise time and a decay time in the $^1G_4$ dynamics, reflecting the Yb^{3+} lifetime and the 75 μs intrinsic lifetime of the $^1G_4$ level. Figure 4 shows that it is not the case and that under Yb^{3+} excitation at 940 nm, the $^1G_4$ dynamics exhibit a sub-10-μs rise time and a decay time as short as 45 μs (Table I).

IV. MODELING

The modeling of the Pr^{3+}-Yb^{3+} system can involve up to 15 energy levels and a great number of possible energy

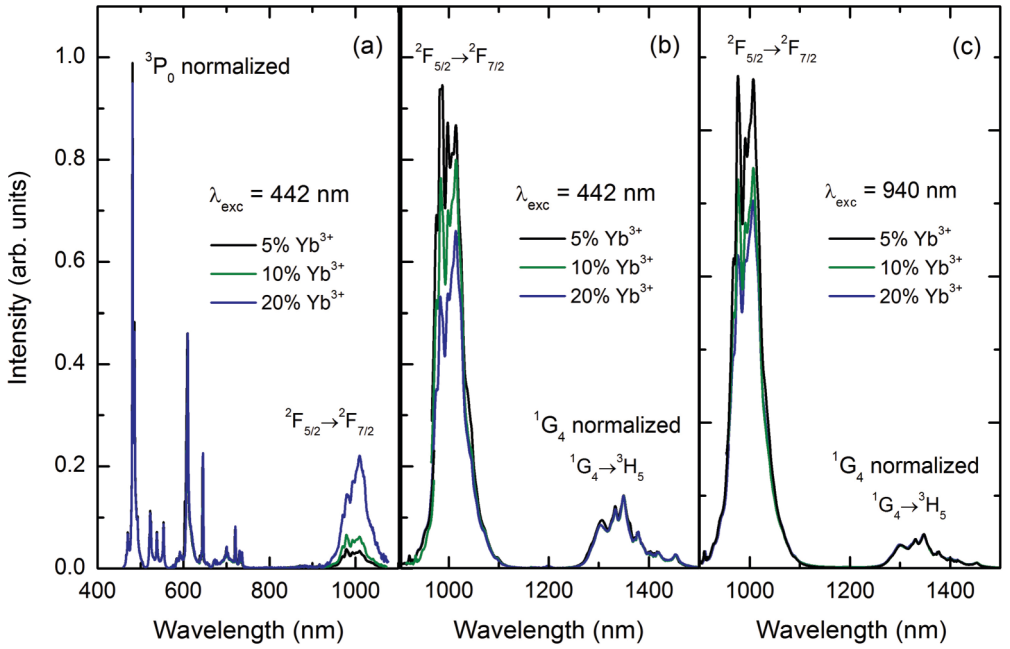

FIG. 3. (Color online) KY_3F_{10}: 0.5%Pr^{3+}-x%Yb^{3+} (x = 5, 10, 20)normalized emission spectra. (a) $^3P_0$ and Yb^{3+} emissions with a normalization on the $^3P_0$ emission spectra, (b) Yb^{3+} and $^1G_4$ emissions under 442-nm excitation with a normalization on the $^1G_4$ emission spectra, and (c) $Yb^{3+}$and $^1G_4$ emissions under 940-nm excitation with a normalization on the $^1G_4$ emission spectra.

transfer processes either by cross-relaxation or upconversion. The purpose of the following modeling is to limit the number of fitting parameters, while being able to describe the various experimental results with good accuracy. This was made possible by restricting the Pr^{3+} energy level scheme, with 13 energy levels, to only three relevant levels, i.e., $^3P_0$, $^1G_4$,

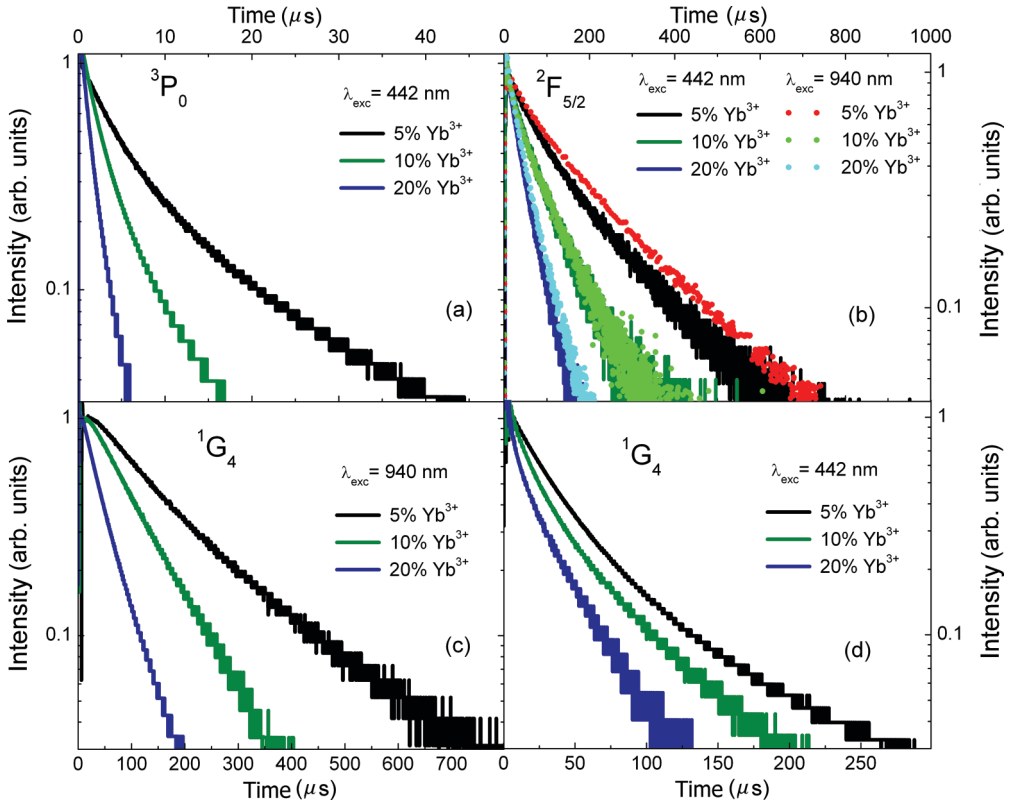

FIG. 4. (Color online) Experimental $^3P_0$, $^1G_4$, and $^2F_{5/2}$ decay curves recorded at 485 nm, 1.35 μm, and 982 nm, respectively, in KY_3F_{10}: 0.5%Pr^{3+}-x%Yb^{3+} (x = 5, 10, 20).

TABLE I. Experimental decay lifetimes. τ_{rt} corresponds to the estimated rise times.

	$\lambda_{exc} = 442$ nm			$\lambda_{exc} = 940$ nm	
Sample	τ^3P_0 (μs)	τ^1G_4(μs)	$\tau^2F_{5/2}$(μs)	τ^1G_4(μs)/τ_{rt} (μs)	$\tau^2F_{5/2}$(μs)
0.5%Pr^{3+}	34	75	–	75	–
0.5%Pr^{3+}-5%Yb^{3+}	8.3	55	154	164/9.4	157
0.5%Pr^{3+}-10%Yb^{3+}	3.0	38	94	95/6.5	80
0.5%Pr^{3+}-20%Yb^{3+}	1.2	19	45	45/2.3	42
0.5%Yb^{3+}	–	–	–	–	1770

and $^3H_4$, provided that some assumptions are verified. First, the $^1D_2$ level can be omitted since the energy gap between $^3P_0$ and $^1D_2$ is high enough (>3500 cm^{-1}) to avoid multiphonon relaxation in a host with low phonon frequency such as KY_3F_{10}. Moreover, the $^3P_0 \rightarrow {}^1D_2$ radiative transition is also known to be very weak so that no significant population is expected in $^1D_2$ when exciting the ^3P_J multiplet. This assumption was verified experimentally as no emission from $^1D_2$ could be detected when exciting the $^3P_2$ multiplet at 442 nm. The $^3P_2$, $^3P_1$, and $^1I_6$ levels undergo fast multiphonon relaxation to $^3P_0$ so that the (^3P_J, $^1I_6$) multiplets are represented by a single level within the model.

In order to avoid upconversion phenomena, all experiments were performed by using low excitation density. A low excitation density allows neglecting any depletion of the $^2F_{7/2}$ and $^3H_4$ ground states. Thus, the ground-state populations in $^3H_4$ and $^2F_{7/2}$ can be reasonably considered equal to the Pr^{3+} and Yb^{3+} dopant concentrations, respectively. For the sake of simplicity, the three energy levels under consideration, i.e., $^3P_0$, $^1G_4$, and $^2F_{5/2}$, are labeled 1, 2, and 3, respectively, in the modeling.

Experimental results were compared to a set of two rate equations when exciting Yb^{3+} ions (system 2) and a set of three rate equations when exciting Pr^{3+} ions (system 3).

$$\frac{dn_2}{dt} = -(R_2 + \beta)n_2 + \gamma n_3 \tag{2a}$$

$$\frac{dn_3}{dt} = -(R_3 + \gamma + \delta)n_3 + \beta n_2 + \sigma\Phi N_{Yb} \tag{2b}$$

$$\frac{dn_1}{dt} = -(R_1 + \alpha)n_1 + \sigma\Phi N_{Pr} \tag{3a}$$

$$\frac{dn_2}{dt} = -(R_2 + \beta)n_2 + \gamma n_3 + \alpha n_1 + R_{12}n_1 \tag{3b}$$

$$\frac{dn_3}{dt} = -(R_3 + \gamma + \delta)n_3 + \beta n_2 + \alpha n_1 \tag{3c}$$

in which n_i is the population of level I, $\sigma\Phi$ represents the pumping rate, with σ the absorption cross section and Φ the excitation photon flux in square centimeter per second. R_i is the decay rate from level i, which is equal to ${\tau_i}^{-1}$, with τ_i the intrinsic lifetime of level i. The parameter R_{ij} corresponds to the radiative decay rate from level i to level j, with $R_{ij} = \beta_R^{ij}\tau_i^{-1}$ and ${\beta_R}^{ij}$ the $i \rightarrow j$ transition branching ratio. α, β, and γ are the energy transfer rates for the QC first transfer, QC second transfer, and backtransfer, respectively (Fig. 5). To avoid any possible confusion, we will further refer to γ as a backtransfer even when considering the excitation of the Yb^{3+} ions (system. 2). As mentioned earlier, the large Yb^{3+} concentration used in the samples, ranging from 5 to 20%, enables energy migration among Yb^{3+} ions, which enhances possible energy transfer towards other impurities, such as Pr^{3+} ion. Therefore, the backtransfer γ from Yb^{3+} towards Pr^{3+} ions is most likely assisted by migration, whereas the first and second QC energy transfers are not, considering the small Pr^{3+} concentration (0.5at.%).

An important issue to address within the modeling is that both Yb^{3+}($^2F_{5/2}$) and Pr^{3+}($^1G_4$) lifetimes (Table I) exhibit a drastic decrease down to 45 μs when exciting Yb^{3+} ions at 940 nm. Such a result cannot be explained by only the transfer (β) from Pr^{3+}($^1G_4$) to Yb^{3+} and the backtransfer (γ). When two energy levels are coupled by such a reciprocal exchange of energy, the decays cannot be shorter than the shortest of both intrinsic Yb^{3+}($^2F_{5/2}$) and Pr^{3+}($^1G_4$) lifetimes; in our case the $^1G_4$ level with a lifetime of 75 μs. This point will be discussed in further detail. Dynamics can, thus, only be described by adding, besides α, β, and γ, a fourth energy transfer mechanism draining the Yb^{3+} excited state, which is related to concentration quenching processes. Like the

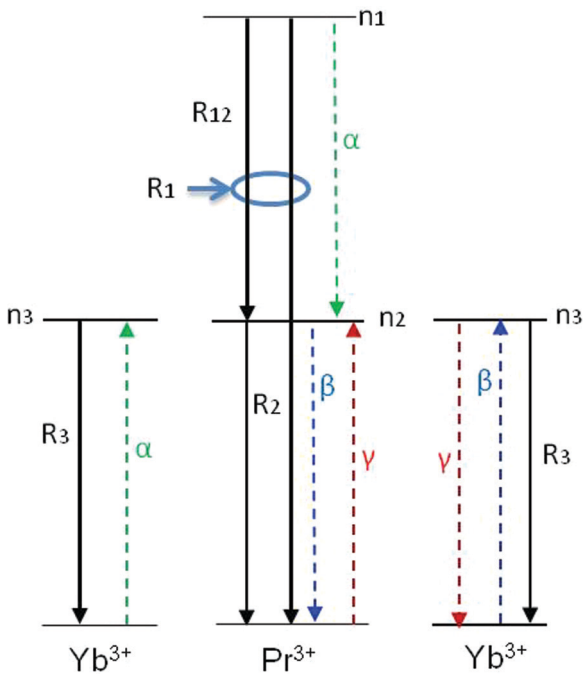

FIG. 5. (Color online) Energy levels and processes involved in downconversion quantum cutting with Pr^{3+} and Yb^{3+} ions. Solid arrows represent radiative transitions and dashed arrows energy transfers.

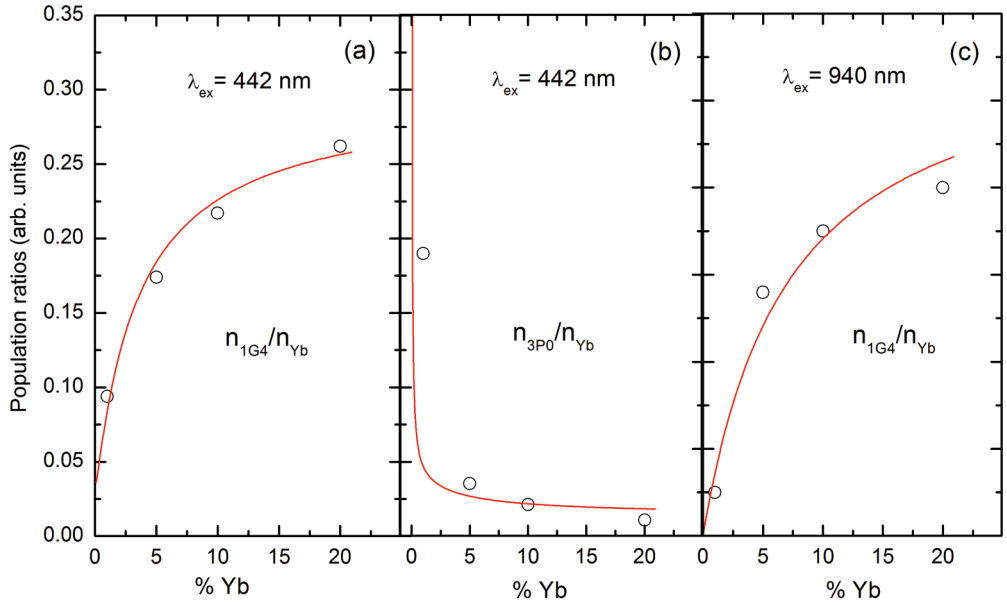

FIG. 6. (Color online) Experimental intensity ratios compared to the simulated population ratios as a function of the Yb^{3+} content.

backtransfer (γ), this concentration quenching mechanism, labeled δ, is assisted by migration among Yb^{3+} ions and is therefore proportional to the donor concentration, i.e., Yb^{3+}. Therefore, energy transfer rates α, β, γ, and δ exhibit the following dependences with the Pr^{3+} and Yb^{3+} concentrations:

$$\alpha = P_\alpha N_{\mathrm{Yb}} \tag{4}$$

$$\beta = P_\beta N_{\mathrm{Yb}} \tag{5}$$

$$\gamma = K_\gamma N_{\mathrm{Yb}} N_{\mathrm{Pr}} \tag{6}$$

$$\delta = P_\delta N_{\mathrm{Yb}} \tag{7}$$

with P_α, P_β, K_γ, and P_δ as the corresponding energy transfer parameters. The backtransfer rate γ in Eq. (6) reflects the typical dependence of migration-assisted energy-transfer rates with both acceptor and donor concentrations,[29,30] while for the concentration quenching δ [Eq. (7)] the acceptor concentration (defects or impurities) is not known.

Systems 2 and 3 were solved under steady-state conditions, $dn_i/dt = 0$, with $i = 1,2,3$. The steady-state equations are used to derive, on one hand, the ratio n_1/n_3 between the $Pr^{3+}(^3P_0)$ and the $Yb^{3+}(^2F_{5/2})$ populations and, on the other hand, the ratio n_2/n_3 between the $Pr^{3+}(^1G_4)$ and the $Yb^{3+}(^2F_{5/2})$ populations. These ratios can be described with rather simple expressions since simplifications occur when calculating the two ratios with systems 2 and 3. When exciting Yb^{3+} ions at 940 nm (system 2), one can derive

$$\frac{n_2}{n_3} = \frac{\gamma}{(R_2 + \beta)} \tag{8}$$

when exciting Pr^{3+} ($^3P_2$) at 442 nm (system 3), one obtains

$$\frac{n_1}{n_3} = \frac{R_2R_3 + \gamma R_2 + \delta R_2 + \beta R_3 + \beta\delta}{\alpha R_2 + \beta R_{12} + 2\alpha\beta} \tag{9}$$

$$\frac{n_2}{n_3} = \frac{R_{12}R_3 + \gamma R_{12} + \delta R_{12} + \alpha R_3 + 2\gamma\alpha + \delta\alpha}{\alpha R_2 + \beta R_{12} + 2\alpha\beta} \tag{10}$$

The dependence of Eqs. (8)–(10) with the Yb^{3+} concentration is easily found by substituting the energy transfer rates α, β, γ, and δ with Eqs. (4)–(7). The dependence of the population ratios with the Yb^{3+} content can actually be compared with the experimental data since the population ratio between two emitting levels is proportional to the corresponding ratio of their emission intensities (Fig. 6). In order to determine experimental intensity ratios, we divided the integrated area of the $^3P_0$ and $^1G_4$ emissions by that of the Yb^{3+} 1-μm emission band (Fig. 3). The increase of the $n(^1G_4)/n(^2F_{5/2})$ ratio with the Yb^{3+} content under Yb^{3+} excitation [Fig. 6(c)] is particularly interesting. This experimental result confirms the need to consider in the modeling that the backtransfer γ is assisted by energy migration among Yb^{3+} ions. Without migration, the backtransfer rate would only depend on the Pr^{3+} concentration and would be, therefore, constant with respect to the Yb^{3+} concentration. Equation (8) would then become

$$\frac{n_2}{n_3} = \frac{\gamma}{(R_2 + P_\beta . N_{\mathrm{Yb}})} \tag{11}$$

which shows that the n_2/n_3 ratio would decrease with the Yb^{3+} concentration in contrast to the observed increase displayed in Fig. 6(c).

In order to confront these experimental results with a modeling with a limited number of fitting parameters, several spectroscopic parameters values are required; i.e., R_1, R_2, R_3, R_{12}, and P_α. The $^3P_0$, $^1G_4$, and $^2F_{5/2}$ intrinsic lifetimes, i.e., without Yb^{3+} codopant (namely, τ_1, τ_2, and τ_3), are equal to 34 μs, 75 μs, and 1.77 ms, respectively (Table I). The branching ratio for the $^3P_0 \rightarrow {}^1G_4$ transition needed for the R_{12} decay rate was experimentally estimated to 3% by recording the $^3P_0$ entire emission spectrum from 480 to 1100 nm, which was then corrected for the spectral response of the setup. The $^3P_0 \rightarrow {}^1D_2$ transition in the infrared was not taken into account as it only gives a small contribution to the overall emission spectrum. The branching ratio β_{12} was then calculated as the ratio between the spectral integral of the

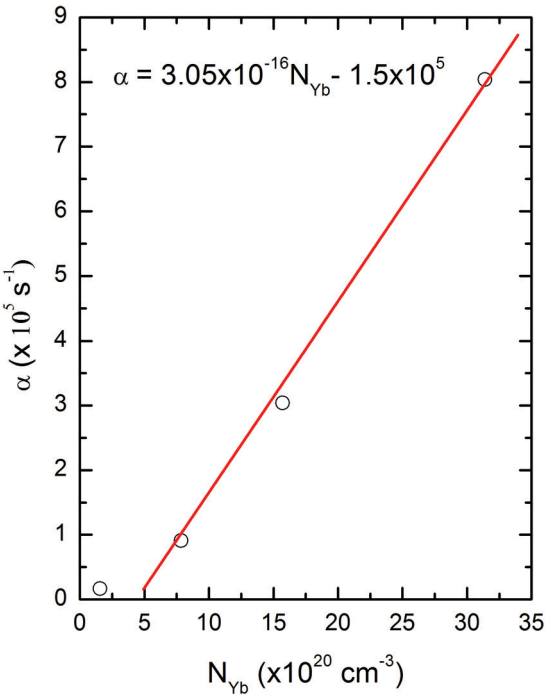

FIG. 7. (Color online) First QC energy transfer rate versus Yb concentration.

$^3P_0 \rightarrow {}^1G_4$ transition of interest and the spectral integral of the $^3P_0$ entire emission spectrum. In contrast with P_β, K_γ, and P_δ, the transfer parameter P_α can be determined quite easily. The energy transfer rate α can be calculated from the experimental data as the difference between the $^3P_0$ total relaxation rate with Yb^{3+} ions $(\tau_{x\%Yb})^{-1}$ and without Yb^{3+} ions $(\tau_0\%Yb)^{-1}$:

$$\alpha = \tau_{x\%Yb}^{-1} - \tau_{0\%Yb}^{-1} \tag{12}$$

following the definition of α given in Eq. (4), P_α can be then derived by linear regression:

$$\tau_{x\%Yb}^{-1} - \tau_{0\%Yb}^{-1} = P_\alpha N_{Yb} \tag{13}$$

Fig. 7 shows the linear fit of the energy transfer rate versus the Yb^{3+} concentration. We obtained $P_\alpha = 3.05 \times 10^{-16}$ cm^3s^{-1}. One can notice that the γ intercept is not 0, showing that the linear dependence of the energy transfer rate with the acceptor concentration [Eq. (11)] is not completely accurate. This nonzero γ intercept might be due to experimental uncertainties related to Yb concentration estimates or lifetime measurements.

It is noteworthy that the three other parameters P_β, K_γ, and P_δ are the only three fitting parameters in the modeling and were adjusted by comparing the modeling and the experimental results, not only the intensity ratios obtained under CW excitation, but also the dynamics obtained under pulsed excitation, both under Yb^{3+} and Pr^{3+} excitations. The best set of parameters values obtained through the fitting procedures and then used throughout this paper is as follows: $P_\beta = 1.34 \times 10^{-17}$ cm^3s^{-1}; $K_\gamma = 4.1 \times 10^{-38}$ cm^6s^{-1}, and $P_\delta = 6.56 \times 10^{-18}$ cm^3s^{-1}. Figure 6 shows that the simulated population ratios as a function of the Yb^{3+} content [Eq. (8) in Fig. 6(c), Eq. (9) in Fig. 6(b), and Eq. (10) in Fig. 6(a)] are in good agreement with the experimental ratios.

Time-dependent solutions of the rate equations in systems 2 and 3 were compared to the experimental decay curves as displayed in Fig. 8. These fluorescence dynamics were obtained under nanosecond pulsed excitation so that the pumping rate $\sigma\Phi$ was considered infinitely short for both systems 2 and 3.

In the case of the Yb^{3+} excitation (system 2), the set of two coupled rate equations can be solved analytically. Closed-form solutions can be then written as follows:

$$n_2(t) = \frac{\gamma}{\sqrt{\Delta}}\left(e^{-\frac{1}{2}(R_2+R_3+\beta+\gamma+\delta-\sqrt{\Delta})t} - e^{-\frac{1}{2}(R_2+R_3+\beta+\gamma+\delta+\sqrt{\Delta})t}\right) \tag{14}$$

$$n_3(t) = \frac{(R_3 - R_2 + \gamma + \delta - \beta + \sqrt{\Delta})}{2\sqrt{\Delta}} e^{-\frac{1}{2}(R_2+R_3+\beta+\gamma+\delta+\sqrt{\Delta})t} - \frac{(R_3 - R_2 + \gamma + \delta - \beta - \sqrt{\Delta})}{2\sqrt{\Delta}} \times e^{-\frac{1}{2}(R_2+R_3+\beta+\gamma+\delta-\sqrt{\Delta})t} \tag{15}$$

in which

$$\sqrt{\Delta} = (R_2 + R_3 + \beta + \gamma + \delta) \times \sqrt{1 - \frac{4(R_2(R_3+\delta+\gamma)+\beta(R_3+\delta))}{(R_2+R_3+\beta+\gamma+\delta)^2}} \tag{16}$$

Eq. (14) was then used to simulate the experimental $^1G_4$ decays [Fig. 4(c)], while Eq. (15) was used to describe the experimental Yb^{3+} decays [Fig. 4(b)], both of them obtained upon Yb^{3+} excitation at 940 nm. Equation (14) for the $^1G_4$ decay exhibits two components: a fast build-up stage with a rate constant $\frac{1}{2}(R_2 + R_3 + \beta + \gamma + \delta + \sqrt{\Delta})$ and an exponential decay with a time constant as follows:

$$\tau = \left(\frac{1}{2}(R_2 + R_3 + \beta + \gamma + \delta - \sqrt{\Delta})\right)^{-1} \tag{17}$$

interestingly, the same time constant appears for the Yb^{3+} fluorescence decay in Eq. (15) and represents the longtime part of this Yb^{3+} decay. Looking in more detail at this common decay time [Eq. (17)], one can see the necessity to take into account the concentration quenching process δ. By considering that this δ mechanism does not exist ($\delta = 0$) and by expanding Eq. (17) in a Taylor series knowing that $(R_2 + R_3 + \beta + \gamma)^2 \gg 4(R_2R_3 + R_3\gamma + \beta R_3)$, the decay rate [Eq. (17)] becomes

$$\tau^{-1} = \frac{(R_2R_3 + R_2\gamma + \beta R_3)}{R_2 + R_3 + \beta + \gamma}. \tag{18}$$

Figure 9 shows the dependence of the decay rate [Eq. (18)] with the energy transfer parameters β and γ. One can see that the maximum value of the decay rate is 13 333 s^{-1}, which is the $^1G_4$ intrinsic (meaning without codopant) decay rate, i.e., $R_2 = (75\ \mu s)^{-1}$. In other words, the shortest $^1G_4$ decay time that can be derived from a model with $\delta = 0$ [Eq. (18)] is equal to the $^1G_4$ intrinsic lifetime, i.e., 75 μs. In fact, the closed expressions Eqs. (14) and(15) with $\delta = 0$ emphasize the fact that when two energy levels are coupled by back and forth energy transfer,

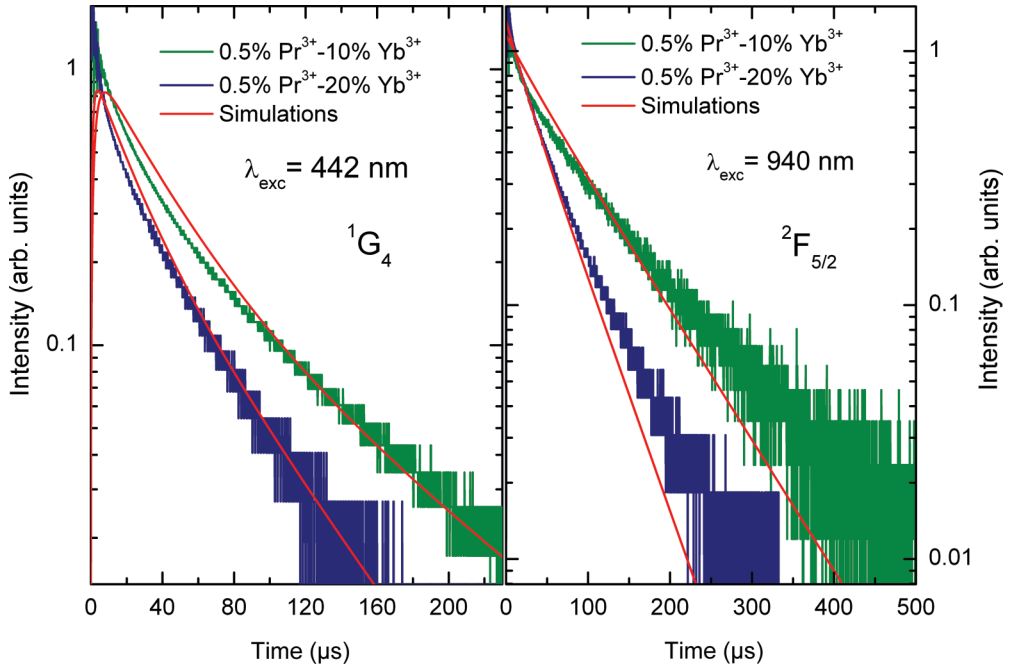

FIG. 8. (Color online) Comparison between experimental and simulated decay curves: (a) ${}^1G_4 \rightarrow {}^3H_5$ decays under 442-nm excitation for the samples doped with 0.5%Pr^{3+} and codoped with 10%Yb^{3+} and 20%Yb^{3+}; and (b) ${}^2F_{5/2} \rightarrow {}^2F_{7/2}$ decays under 940-nm excitation for the samples doped with 0.5%Pr^{3+} and codoped with 10%$Yb^{3+}$and 20%Yb^{3+}.

the longtime part of their respective dynamics will reflect the values of their intrinsic lifetimes. This limitation makes the model with $\delta = 0$ unable to explain the measured lifetimes of 45 μs for ${}^1G_4$ in KY_3F_{10}: 0.5%Pr^{3+}-20%Yb^{3+} (Table I). The introduction into the modeling of the concentration quenching δ mechanism, which does not take part in the mutual energy exchange, reduces the simulated Yb^{3+} emission lifetime and consequently the ${}^1G_4$ decay time.

Using the same four energy transfer parameters values, $P_\alpha = 3.05 \times 10^{-16}$ cm^3s^{-1}; $P_\beta = 1.34 \times 10^{-17} cm^3s^{-1}$; $K_\gamma = 4.1 \times 10^{-38}$ cm^6s^{-1}, and $P_\delta = 6.56 \times 10^{18}$ $cm^{-3}s^{-1}$, as in the modeling of the intensity ratios, Eqs. (14) and (15) can successfully reproduce the experimental ${}^1G_4$ and ${}^2F_{5/2}$ lifetimes upon ir excitation at 940 nm, as shown in Fig. 8. In the case of ${}^3P_0$ excitation at 442-nm, closed expressions

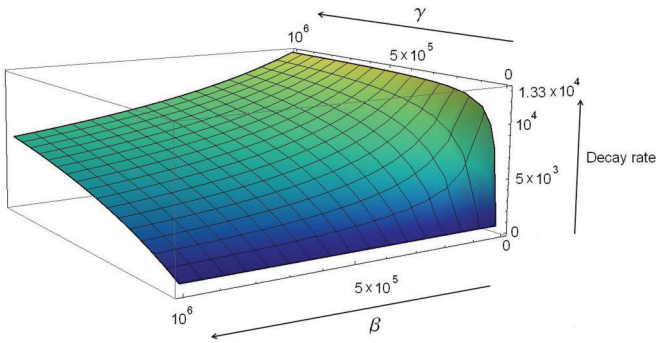

FIG. 9. (Color online) Decay rate (s^{-1}) as in Eq. (18) with β and γ varying from 0 to 10^6 s^{-1}. The decay rate approaches asymptotic values equal to 13 333 s^{-1} ($= R_2$) and 6949 s^{-1} [$=(R_2 + R_3)/2$] and 542 s^{-1} [$= (R_2R_3)/(R_2 + R_3)$] at the limits ($\beta \rightarrow 0, \gamma \rightarrow \infty$), ($\beta \rightarrow \infty, \gamma \rightarrow \infty$), and ($\beta \rightarrow 0, \gamma \rightarrow 0$), respectively.

could not be easily found as it involves a set of three-coupled rate equations (system 3). Numerical solutions were, thus, found again with the same four-energy transfer parameters. A general good agreement (Table II) is found between the average lifetimes [Eq. (1)] derived from the modeling and the experimental values. While the modeling is able to derive the average lifetimes of the different levels, the exact shape of the decays is more difficult to reproduce, as illustrated in Fig. 8 in two different cases.

V. DISCUSSION

Our modeling shows that the interpretation of the different experimental results must be handled with care as the Pr^{3+}-Yb^{3+} system involves four different energy transfers. In particular, the Yb^{3+} emission intensity, which needs to be as strong as possible for a practical application of KY_3F_{10}: Pr^{3+}-Yb^{3+} as a solar quantum cutter, is the result of two feeding energy transfers (α from the ${}^3P_0$ level and β from the ${}^1G_4$ level) and two quenching processes (backtransfer γ towards the ${}^1G_4$ level and concentration quenching δ). The system is made even more complicated as the β and γ

TABLE II. Comparison between theoretical (Th) and experimental (Exp) lifetimes.

	$\lambda_{ex} = 442$ nm			$\lambda_{ex} = 940$ nm	
	$\tau_{3P0}(\mu s)$	$\tau_{1G4}(\mu s)$	$\tau_{Yb}(\mu s)$	$\tau_{1G4}(\mu s)$	$\tau_{Yb}(\mu s)$
Sample	Th/Exp	Th/Exp	Th/Exp	Th/Exp	Th/Exp
0.5%Pr^{3+}-5%Yb^{3+}	8.4/8.3	54/55	155/154	155/164	151/157
0.5%Pr^{3+}-10%Yb^{3+}	2.8/3.0	42/38	94/94	94/95	85/80
0.5%Pr^{3+}-20%Yb^{3+}	1.2/1.2	28/19	49/50	49/45	40/42

TABLE III. Energy transfer rates in KY_3F_{10} codoped with Pr^{3+} and Yb^{3+} ions.

Sample	α (s^{-1})	β (s^{-1})	γ (s^{-1})	δ (s^{-1})
0.5%Pr^{3+}-5%Yb^{3+}	8.95×10^4	1.05×10^4	2.5×10^3	5.05×10^3
0.5%Pr^{3+}-10%Yb^{3+}	3.3×10^5	2.1×10^4	5.05×10^3	1.0×10^4
0.5%Pr^{3+}-20%Yb^{3+}	8.1×10^5	4.2×10^4	1.0×10^4	2.0×10^4

energy transfers go back and forth between the $^1G_4$ and the $^2F_{5/2}$ levels, creating a population equilibrium between these two levels. Therefore, the determination of the QC process efficiency is not straightforward. Some reports use only the ETE of the QC first step to derive the quantum efficiency of the whole QC process by assuming implicitly that the QC second step has a 100% efficiency or that the QC is merely a cooperative process.[17] With these assumptions, the QC efficiency can be easily expressed as follows:

$$\eta_{QC} = \eta_{r(3P0)}(1 - \eta_{x\%Yb(1)}) + 2\eta_{x\%Yb(1)} \tag{19}$$

in which $\eta_{x\%Yb(1)}$ is the ETE for the QC first energy transfer and $\eta_{r(3P0)}$ is the $^3P_0$ intrinsic radiative quantum efficiency, which is usually set to 1 in low phonon energy hosts. The assumptions needed to use Eq. (19) seem, however, excessive. A cooperative process only takes place when the first-order processes can be neglected, and this is not the case of the Pr^{3+}-Yb^{3+} system.[16] It is, however, possible to derive a more realistic QC efficiency, taking into account all the possible energy transfers by calculating their respective energy transfer rates.

Table III presents the energy transfer rates derived from the transfer parameters (P_β, P_α, K_γ, and P_δ) for the different samples. One can notice that the largest energy transfer rates are obtained for α, the QC first energy transfer, reaching 8.08×10^5 s^{-1} in 0.5%Pr^{3+}-20%Yb^{3+}: KY_3F_{10}. From these energy transfer rates, one can easily derive ETEs. The ETE is defined in a general way as the ratio between the energy transfer rate and the total relaxation rate, comprising energy transfer, radiative decay, and the multiphonon relaxation rates. We can, thus, derive for the QC first and second energy transfer the corresponding ETE $\eta_{x\%Yb(1)}$ and $\eta_{x\%Yb(2)}$, respectively, as follows:

$$\eta_{x\%Yb(1)} = \frac{\alpha}{\alpha + \tau_{1-0\%Yb}^{-1}} \tag{20}$$

$$\eta_{x\%Yb(2)} = \frac{\beta}{\beta + \tau_{2-0\%Yb}^{-1}} \tag{21}$$

in which $\tau_{1-0\%Yb}$ and $\tau_{2-0\%Yb}$ are the intrinsic relaxation rates of $^3P_0$ and $^1G_4$, respectively (Table I). These two ETE values (Table IV) can then be combined to derive an intrinsic QCE, which takes into account the ETE of both first and second QC energy transfers, but not the Yb^{3+} emission quenching processes, as follows,

$$\eta_{QC} = \eta_{r(3P0)}(1 - \eta_{x\%Yb(1)}) + \eta_{x\%Yb(1)} + \eta_{x\%Yb(1)}[\eta_{r(1G4)}(1 - \eta_{x\%Yb(2)}) + \eta_{x\%Yb(2)}] \tag{22}$$

in which the term $\eta_{r(1G4)}(1 - \eta_{x\%Yb(2)})$ represents the contribution of photons emitted by the $^1G_4$ level. However, these photons will hardly be useful for a Si solar cell since the $^1G_4$ level emission around 1 μm is very limited. By neglecting this contribution of useless photons in Eq. (22) and setting $\eta_{r(3P0)}$ equal to 1, one can obtain a much simpler expression for the QCE:

$$\eta_{QC} = 1 + \eta_{x\%Yb(1)}.\eta_{x\%Yb(2)}. \tag{23}$$

The corresponding results are presented in Table IV. As expected, the QCE increases with the Yb^{3+} concentration since the two consecutive QC energy transfers become more efficient. These ideal QCE values, which do not take into account the backtransfer γ and the concentration quenching δ processes, are as high as 173% in KY_3F_{10}: 0.5%Pr^{3+}-20%Yb^{3+}. Interestingly, Eq. (23) represents what can be observed experimentally by excitation spectroscopy when comparing the excitation spectra of the Yb^{3+} emission in singly Pr^{3+} doped and Pr^{3+}-Yb^{3+} codoped samples .[8,20] The comparison between the excitation into the $^1D_2$ and the $^3P_0$ levels reveal a drastic increase of the Yb^{3+} emission when exciting the $^3P_0$ level because of the two-step energy transfer towards Yb^{3+} ions. In these types of experiments, one can observe the effect of the two consecutive QC energy transfers without directly observing the Yb^{3+} quenching mechanisms since the Yb^{3+} emission is quenched the same way whether the excitation is performed on the $^1D_2$ or the $^3P_0$ levels. In other words, the quenching mechanisms are present but cannot be observed when only comparing an excitation in the $^1D_2$ and the $^3P_0$ levels.

It is, however, possible to further modify Eq. (22) to encompass these quenching mechanisms by using the Yb^{3+} radiative quantum efficiency, which can be defined as

$$\eta_{rYb} = \frac{\tau_{Yb0}^{-1}}{\delta + \gamma + \tau_{Yb0}^{-1}} \tag{24}$$

in which τ_{Yb0} is the radiative lifetime of the $^2F_{5/2}$ level (τ = 1.77 ms). Eq. (22) can then be rewritten, again with $\eta_{r(3P0)} = 1$ and $\eta_{r(1G4)}(1 - \eta_{x\%Yb(2)}) = 0$ to define a more realistic QCE where the quenching of the Yb^{3+} emission directly affects the excited Yb^{3+} ions:

$$\eta_{QC} = (1 - \eta_{x\%Yb(1)}) + \eta_{x\%Yb(1)}.\eta_{rYb} + \eta_{x\%Yb(1)}.\eta_{x\%Yb(2)}.\eta_{rYb}. \tag{25}$$

Results obtained with Eq. (25) are displayed in Table IV showing clearly the tremendous impact of the Yb^{3+} quenching mechanisms, which drastically reduces the 1 μm Yb^{3+} emission and consequently the overall efficiency of the system. The QCE values range from 32 to 6.2% and are consistent with the 12% QCE measured using an integrating sphere.[21] Energy migration among Yb^{3+} ions leads to the increase of the backtransfer γ and the concentration quenching δ efficiency with the Yb^{3+} content. This increase prevails over

TABLE IV. ETEs and QCE.

Sample	ETE [Eq. (20)] (%)	ETE [Eq. (21)] (%)	QCE (%) [Eq. (23)]	QCE (%) [Eq. (25)]
$0.5\%Pr^{3+}$-$5\%Yb^{3+}$	75.6	44.0	133	32
$0.5\%Pr^{3+}$-$10\%Yb^{3+}$	91.4	61.2	156	14
$0.5\%Pr^{3+}$-$20\%Yb^{3+}$	96.9	75.9	173	6.2

the corresponding increase of the intrinsic QC efficiency, which is observed with Eq. (23).

VI. CONCLUSION

The development of quantum cutters leading to the splitting of one visible photon into two infrared photons is an interesting way of reducing the thermalization losses observed in Si solar cells. A rate equation modeling of the QC process in the Pr^{3+}-Yb^{3+} system with four major energy transfers (two QC feeding transfers and two quenching processes) was developed to describe the different fluorescence dynamics of Pr^{3+} and Yb^{3+} ions, along with the Pr^{3+} and Yb^{3+} intensity ratios obtained under CW excitation. The number of adjusting parameters was intentionally kept to a minimum in order to build a realistic modeling. Other energy transfers, such as upconversion mechanisms, could be taken into account but have a limited impact on the experimental results since the excitation density was kept below the onset level of observable upconversion luminescence. The overall agreement between the experiments and the modeling is quite satisfactory considering that the modeling was confronted with different sets of experiments under CW and pulsed excitations of both Pr^{3+} and Yb^{3+} ions. The modeling shows that while the two-step energy transfer from Pr^{3+} to Yb^{3+} truly takes place with a maximum efficiency of 173% in KY_3F_{10}: $0.5\%Pr^{3+}$-$20\%Yb^{3+}$, the overall QC efficiency in terms of 1-μm output photons is considerably reduced by energy backtransfer processes from Yb^{3+} to Pr^{3+} and concentration quenching mechanisms affecting the Yb^{3+} emission, which degrades the QCE in this sample down to 6.2%. Very high QC efficiency values, found in the literature based on spectroscopic experiments, are in agreement with our findings that the two step QC mechanism is, in fact, efficient, but these experiments do not take into account quenching processes. Experimental results can only be accurately described by taking into account energy migration among Yb^{3+} ions, which further enhances the detrimental effect of the quenching processes. As a result, the migration-assisted quenching processes become more efficient with the Yb^{3+} concentration, leading to the decrease of the overall QCE efficiency with the Yb^{3+} content. These competing processes drastically limit the efficiency of the Pr^{3+}-Yb^{3+} system within the 1-μm spectral window which is the spectral target for Si-based solar applications.

*Corresponding author: alain.braud@ensicaen.fr

[1]W. Shockley and H. J. Queisser, J. Appl. Phys. **32**, 510 (1961).
[2]T. Trupke, M. A. Green, and P. Würfel, J. Appl. Phys. **92**, 1668 (2002).
[3]R. T. Wegh, H. Donker, and A. Meijerink, Phys. Rev. B **56**, 13841 (1997).
[4]R. T. Wegh, H. Donker, K. D. Oskam, and A. Meijerink, J. Lumin. **82**, 93 (1999).
[5]B. Liu, Y. Chen, C. Shi, H. Tang, and Y. Tao, J. Lumin. **101**, 155 (2003).
[6]J.-M. Meijer, L. Aarts, B. M. van der Ende, T. J. H. Vlugt, and A. Meijerink, Phys. Rev. B **81**, 035107 (2010).
[7]L. Aarts, S. Jaeqx, B. M. van der Ende, and A. Meijerink, J. Lumin. **131**, 608 (2011).
[8]B. M. van der Ende, L. Aarts, and A. Meijerink, Adv. Mater. **21**, 3073 (2009).
[9]G. Lakshminarayana, H. Yang, S. Ye, Y. Liu, and J. Qiu, J. Phys. D **41**, 175111 (2008).
[10]L. Xie, Y. Wang, and H. Zhang, Appl. Phys. Lett. **94**, 061905 (2009).
[11]P. Vergeer, T. J. H. Vlugt, M. H. F. Kox, M. I. den Hertog, J. P. J. M. van der Eerden, and A. Meijerink, Phys. Rev. B **71**, 014119 (2005).
[12]F. Auzel, Chem. Rev. **104**, 139 (2004).
[13]D. Serrano, A. Braud, J.-L. Doualan, P. Camy, A. Benayad, V. Ménard, and R. Moncorgé, Opt. Mater. **33**, 1028 (2011).
[14]D. Serrano, A. Braud, J.-L. Doualan, P. Camy, and R. Moncorgé, J. Opt. Soc. Am. B **28**, 1760 (2011).
[15]K. Deng, X. Wei, X. Wang, Y. Chen, and M. Yin, App. Phys. B **102**, 555 (2011).
[16]J. T. van Wijngaarden, S. Scheidelaar, T. J. H. Vlugt, M. F. Reid, and A. Meijerink, Phys. Rev. B **81**, 155112 (2010).
[17]Q. Y. Zhang and G. F. Yang, Appl. Phys. Lett. **91**, 051903 (2007).
[18]A. Jaffrès, B. Viana, and E. van der Kolk, Chem. Phys. Lett. **527**, 42 (2012).
[19]X. Liu, Y. Qiao, G. Dong, S. Ye, B. Zhu, G. Lakshminarayana, D. Chen, and J. Qiu, Opt. Lett. **33**, 2858 (2008).
[20]A. Guille, A. Pereira, C. Martinet, and B. Moine, Opt. Lett. **37**, 2280 (2012).
[21]Y. S. Xu, X. H. Zhang, S. X. Dai, B. Fan, H. L. Ma, J. L. Adam, J. Ren, and G. R. Chen, J. Phys. Chem. C **115**, 13056 (2011).
[22]E. van der Kolk, O. M. T. Kate, J. W. Wiegman, D. Biner, and K. W. Krämer, Opt. Mater. **33**, 1024 (2011).
[23]S. A. Payne, L. K. Smith, W. L. Kway, J. B. Tassano, and W. F. Krupke, J. Phys.: Condens. Matter **4**, 8525 (1992).

[24]P. Porcher and P. Caro, J. Chem. Phys. **65**, 89 (1976).
[25]A. Braud, P. Y. Tigreat, J. L. Doualan, and R. Moncorgé, Appl. Phys. B: Lasers Opt. **72**, 909 (2001).
[26]A. Yoshikawa, K. Kamada, M. Nikl, K. Aoki, H. Sato, J. Pejchal, and T. Fukuda, J. Cryst. Growth **285**, 445 (2005).
[27]M. Ito, G. Boulon, A. Bensalah, Y. Guyot, C. Goutaudier, and H. Sato, J. Opt. Soc. Am. B **24**, 3023 (2007).
[28]D. Serrano, A. Braud, J.-L. Doualan, P. Camy, and R. Moncorgé, J. Opt. Soc. Am. B **29**, 1854 (2012).
[29]M. Yokota and O. Tanimoto, J. Phys. Soc. Jpn. **22**, 779 (1967).
[30]A. I. Burshtein, J. Lumin. **21**, 317 (1980).